

Conductance response of graphene nanoribbons and quantum point contacts in the scanning gate measurements

A. Mreńca, K. Kolasinski, and B. Szafran
 AGH University of Science and Technology,
 Faculty of Physics and Applied Computer Science,
 al. Mickiewicza 30, 30-059 Kraków, Poland

We provide a theoretical study of the conductance response of systems based on graphene nanoribbon to the potential of a scanning probe. The study is based on the Landauer approach for the tight-binding Hamiltonian with an implementation of the quantum transmitting boundary method and covers homogenous nanoribbons, their asymmetric narrowing and quantum point contacts of various profiles. The response maps at low Fermi energies resolve formation of n-p junctions induced by the probe potential and a presence of zigzag-armchair segments of the edges for inhomogeneous ribbons. For an asymmetric narrowing of the nanoribbons the scanning probe resolves formation of standing waves related to backscattering within the highest subband of the narrower part of the system. The QPCs containing a long constriction support formation of localized resonances which induce a system of conductance peaks that is reentrant in the Fermi energy, with the form of the probability density that can be resolved by the conductance mapping. For shorter constrictions the probe induces smooth conductance minima within the constrictions. In general, besides the low-energy transport gap, in the wider parts of the ribbon the variation of the conductance of the system is low compared to the narrower part.

I. INTRODUCTION

The electron flow in semiconductor nanostructures containing a two-dimensional electron gas (2DEG) buried shallow beneath the surface of the structure can be probed by a charged tip of an atomic force microscope. The technique, known as the scanning gate microscopy¹ (SGM), gathers conductance maps as functions of the position of the tip that is capacitively coupled to the electron gas. For 2DEG confined in bulk semiconductors the maps are used to extract electron trajectories², branching of the electron flow via quantum point contacts (QPCs)³, many-body phenomena⁴, Aharonov-Bohm effects⁵ and scarred wave functions in quantum billiards⁶ as well as the interference effects³ due to backscattering by the tip. The SGM technique has also been used⁷⁻¹³ for graphene with the electron gas remaining strictly on the surface of the structure. In particular, SGM technique was applied in studies of charge inhomogeneities^{7,8}, charging localized states formed within a widening of the nanoribbons⁹ and at potential constrictions¹⁰, universal conductance fluctuations¹¹ and weak localization effects¹². Very recently a SGM study of the graphene quantum rings was reported¹³ with conductance fringes as due to resonant localized states.

Quantum point contacts are basic elements of the quantum transport circuitry allowing for the current injection and detection, control of the number of conducting of modes, etc. The conductance quantization for QPCs defined within the bulk semiconductors is usually observed for electrostatic potentials¹⁴ controlling the width of the constriction. For graphene systems this approach is rather excluded, since the Klein tunneling^{15,16} and perfectly conducting channels^{17,18} in graphene nanoribbons lead to a low effectiveness of electrostatic confinement and backscattering, allowing the

Dirac electrons to pass across potential barriers¹⁹. The QPCs are therefore formed by tailoring constrictions²⁰⁻²² of the nanoribbons^{23-27,29-31}. The ineffectiveness of backscattering in graphene seems reflected by the results of the experimental SGM studies of the quantum point contacts (QPC)^{10,32} which find flat conductance maps outside the QPC³² in a distinct contrast to the results obtained for bulk semiconductor in which interference fringes due to the backscattering by the tip and the resulting formation of standing wave between the QPC and the probe are clearly observed³. The scanning gate microscopy was used³³ for detection of spontaneous quantum dots formed along the disordered ribbon within the transport gap²³.

The purpose of the present paper is to determine the response of graphene quantum point contacts formed by constrictions of the nanoribbons to the scanning probe [Fig. 1(c)]. As a starting point of the study we consider reaction of homogenous graphene nanoribbons [Fig. 1(a)] to the perturbation by an external potential and asymmetric narrowing [Fig. 1 (b)] of the channels³⁴. The QPC [Fig. 1(c)] is formed by two asymmetric connections [Fig. 1(b)], whose scattering properties and response to the probe needs to be determined in order to separate the effects of the resonances formed within the QPC. We consider systems of perfect armchair or zigzag edges – and systems varying with atomic-step edges, as can be produced with the Joule heating technique³⁵. For pristine graphene ribbons²³⁻²⁵ the edge determines the character of the ribbon (semiconducting or semimetallic) and the ribbons with boundaries other than armchair have the transport properties similar to the zigzag edges³⁶. For the purpose of the present study we develop an implementation of the quantum transmitting boundary³⁷ method for the solution of the coherent transport problem set by scattering solution of the Schrödinger equation

for the tight-binding Hamiltonian. We study both the effects of the local potential variation induced by the tip on edge-localized states and the effects of backscattering within the constrictions. For QPCs the scattering induced by disorder³ and the inhomogeneity of the edges³⁹ destroy the conductance quantization which can still be observed²¹ for mesoscopically smooth boundaries²² of the constriction. As compared to QPCs, we find that an asymmetric narrowing, i.e. a contact between nanoribbons of varied width, exhibits a very clear conductance quantization as a function of the Fermi energy, also when the edges are not smooth at the mesoscopic scale. We study quantum point contacts and find that for short constrictions there is a flat minimum of conductance for the tip above the constriction in agreement with the results of Ref.³². Generally, for any tip potential we find that outside the graphene constrictions the variation of the conductance by the tip potential is not pronounced as in the experiments of Refs.^{10,32}. For longer constrictions however a regular formation of the standing waves occurs which – according to the present study – should be resolved by the scanning gate microscopy.

The resonant states localized at armchair-zigzag connections at ribbon constrictions formed by atomic steps^{22,40} induce a strong backscattering. These resonant states quench the conductance to zero at low energy. We find that the charge transport can be unblocked by the potential of the probe which neutralizes the scattering centers, with conductance maps forming halos similar to those found in the Coulomb blockade experiment of Ref.¹⁰. The response for homogenous nanoribbons to the probe potential at low Fermi energies is determined by the existence of perfectly conducting channels (metallic armchair and zigzag ribbons), as well as by formation of local n-p junctions at the edges (zigzag ribbons).

This paper is organized as follows: in Section II we outline the calculation method which is described in detail in the Appendix, Section III, IV and V describe the response of the nanoribbons, their narrowing and constrictions, respectively (see Fig. 1). Summary and conclusions are given in Section VI.

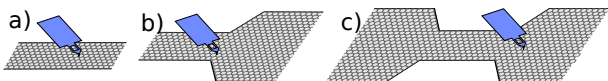


FIG. 1: Schematic drawing of the systems studied: nanoribbon (a), asymmetric narrowing (b) and QPC (c).

II. METHOD

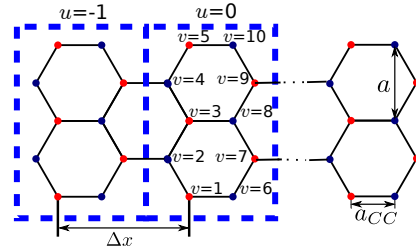


FIG. 2: Schematic drawing of the nanoribbons in the input and output channels. In the Bloch waves that serve as the eigenstates of the channels u numbers the elementary cells, v the ions within the cell $a_{CC} = 0.142$ nm is the nearest neighbor distance, $a = 0.246$ nm is the lattice constant, and Δx is the period of the considered nanoribbon.

We use the tight binding Hamiltonian for π electrons with the nearest neighbor hopping

$$H = \sum_{\{i,j\}} t_{ij} (c_i^\dagger c_j + c_j^\dagger c_i) + \sum_i V(\mathbf{r}_i) c_i^\dagger c_i, \quad (1)$$

and the hopping energy of $t_{ij} = -2.7$ eV. For the description of the transport at the Fermi level we prepared a tight-binding version of the quantum transmitting boundary method³⁷ (for the finite difference approach see Ref.⁴¹). The studied system consists of an input and output channels and a scattering region. We assume that the channels are infinite and uniform, i.e. periodic in the atomic scale. The electron eigenstates in the nanoribbons are determined in the Bloch form,

$$\psi_{u,v}^k = \chi_v^k e^{iku\Delta x}, \quad (2)$$

where k is the wave vector, u numbers the elementary cells of the ribbon (see Fig. 2), v – the atoms within the elementary cell, and χ_v^k is the periodic function, assuming the same values within each elementary cell of the ribbon. The detailed procedure for determining the dispersion relation and Bloch functions for the channels is given in the Appendix.

Generally, in the Hamiltonian eigenstates within the channels the scattering wave function is a linear combination of the Bloch functions for a number of subbands at the Fermi level

$$\psi_{u,v} = \sum_l (c_{in}^l \chi_v^{k_+^l} e^{ik_+^l u \Delta x} + d_{in}^l \chi_v^{k_-^l} e^{ik_-^l u \Delta x}). \quad (3)$$

For the electron incident to the scattering region from the left in the input (left) lead far away from the scattering region the electron wave function takes the form of a superposition of incoming (k_+) and backscattered (k_-) Bloch waves,

$$\psi_{0,v} = \sum_l (c_{in}^l \chi_v^{k_+^l} + d_{in}^l \chi_v^{k_-^l}), \quad (4)$$

where c_{in}^l are the amplitudes of the incoming states and d_{in}^l - of the outgoing ones. The sum in Eq. (4) runs over the current carrying states since at a large distance from the scatterers the contribution of the evanescent modes can be neglected. In the right lead the wave function is a superposition of Bloch waves traveling from the scattering region,

$$\psi_{N,v} = \sum_l c_{out}^l \chi_v^{k_+^l} e^{ik_+^l N \Delta x}. \quad (5)$$

For solution of the scattering problem we assume that the electron is incident in a single subband l , $c_{in}^l = \delta_{jl}$. Then, the amplitudes d_{in}^l and c_{out}^l are to be determined. At the boundaries between the leads and the scattering region which we cover within the computational box we require continuity of both of the wave function and its derivative. The numerical procedure for determination of the scattering amplitudes is given in the Appendix.

Once the scattering amplitudes are determined we proceed to calculation of transmission T and reflection R probabilities for the i th incident mode according to the Landauer approach^{42,43}, $T_i = \sum_j t_{ij}$ and $R_i = \sum_j r_{ij}$,

where $t_{ij} = \left| \frac{c_{out}^j}{c_{in}^i} \right|^2 \left| \frac{(\phi_{k_+})^j}{(\phi_{k_+})^i} \right|^2$ and $r_{ij} = \left| \frac{d_{in}^j}{c_{in}^i} \right|^2 \left| \frac{(\phi_{k_-})^j}{(\phi_{k_+})^i} \right|^2$, are the probabilities of the electron transfer from incident subband i to j subband of the output and input channels, respectively, and $(\phi_{k_+})^i$ [$(\phi_{k_-})^i$] is the probability current flux of the i th mode wave function traveling in the right [left] direction.

The currents in the tight binding approach flow along the π interatomic bonds, and the formula for the current flowing from atom m to atom n as derived⁴⁴ from the Schrödinger equation is

$$j_{mn} = \frac{i}{\hbar} [t_{mn} \psi_m^* \psi_n - t_{nm} \psi_n \psi_m^*], \quad (6)$$

where ψ_m is the wave function at the m -th ion. The flux is evaluated as

$$\phi = \sum_l \sum_{n_l} j_{ln_l}, \quad (7)$$

where the sum runs over the atoms across the end of the channel l and their neighbors n_l within the interior of the computational box. Finally, the conductance is evaluated from the Landauer formula as $G = \frac{2e^2}{h} \sum_i T_i$. Since the formula involves sum over incident subbands, for the calculations it is sufficient to consider the solution of the Schrödinger equation for a single input channel only. Note, that our choice of the quantum transparent boundary conditions implies working with the wave functions - which is an alternative to the Greens function method^{19,38}, that deals with Hamiltonian operators mainly. The choice between the two is a matter of taste.

The effective potential of the charged tip as seen by the Fermi level electrons is a result of the screening of its

Coulomb potential by the electron gas. The effective potential as obtained by the Schödinger-Poisson modeling⁴⁵ can be approximated by a Lorentz function

$$V(x, y) = \frac{V_t}{1 + ((x - x_t)^2 + (y - y_t)^2) / d^2}, \quad (8)$$

where x_t, y_t are the coordinates of the tip position, d - the width of the effective tip potential and V_t - its height. The height of the tip potential is determined by the charge accumulated by the tip, and d is of the range of the tip - electron gas distance⁴⁵. A discussion of the results for varied V_t and d parameters is provided below.

III. CONDUCTANCE MAPPING FOR NANORIBBONS

We consider first the zigzag ribbons - labeled by ZZ in the Figures, and next proceed to armchair: semiconducting (AS) and metallic (AM) ribbons.

A. Zigzag ribbons

Figure 3(a) shows the dispersion relation for a zigzag nanoribbon with 102 atoms across the channel. The zigzag edge does not couple the states of the K and K' valleys of graphene which are thus present in the dispersion relation ($K, K' = \pm \frac{2\pi}{3a}$). The dispersion relation is given in Figs. 3(a-c). For Fermi energy $E_F = 0.44$ eV there are five eigenstates with current flowing to the right ($k_{1'_+}, k_{2'_+}, k_{3'_+}, k_{2_+}, k_{3_+}$) and to the left ($k_{1_-}, k_{2'_-}, k_{3'_-}, k_{2_-}, k_{3_-}$).

Let us consider the ribbons conductance response to the tip potential for a low energy of the incident electron. Figures 4(a-b) show the transfer probability as a function of the tip position across the ribbon for two values of E_F corresponding to the lowest subband transport (electron incoming with wave vector $k_{1'_+}$, that can be backscattered only to k_{1_-} - see Fig. 3(b,c)). For both the considered Fermi energies the conductance gets low when the tip is located near the edge, in spite of the fact that the current for the unperturbed zigzag ribbon vanishes at the edges [Figure 4(d-e)]: at the zigzag edges only the ions of a single sublattice are occupied in the Hamiltonian eigenstates [Figure 4(g-h)] and the current flows between the ions belonging to different sublattices²⁶. For the central position of the tip we have either $T = 1$ for larger $E_F = 0.13$ eV [Fig. 4(b)] or a rapid variation of T between 0 and 1 for the lower $E_F = 0.07$ eV [Fig. 4(a)]. In the plot of G as a function of the tip position and the Fermi energy given in Fig. 5 we find a wedge-shaped flat region with $T = 1$. This region is related to the perfectly conducting channel^{17,18} in the zigzag ribbon. Perturbation by the tip - even if large - does not induce scattering between the K and K' valleys as long as the tip potential is slowly varying at the atomic scale. Since the tip potential has a long range character there is no intervalley

scattering, and in consequence – in the lowest subband transport conditions – the backscattering is absent, unless the tip is located near the edge of the ribbon [cf. Fig. 6]. The tip – placed in the center of the ribbon – is not exactly transparent for the electron flow, since the current makes its way between the edge [Figure 7(a)], but anyway no conductance response is observed. For the tip near the edge, the current circulates around the defect before it is backscattered (see Fig. 7(b) – the illustrated case corresponds to $T = 0$). The edge mediates in the intervalley scattering provided that its potential is raised to the Fermi energy⁴⁶ by e.g. the tip inducing formation of a local n-p junction. In Fig. 5 we marked with the black line the position of the tip for which its potential at the lower ribbon edge is raised to the Fermi energy, with a perfect agreement with the boundaries of $T = 1$ wedge region. The transfer probability as a function of the tip position plotted in Fig. 4(a) for low E_F exhibits a rapid variation between 0 and 1 which corresponds to the case when the tip potential at *both* edges exceeds E_F , hence multiple intervalley scattering events occur, resulting in either $T = 0$ or $T = 1$.

The $T = 1$ wedge region continues smoothly into the regime of a few transport subbands at the Fermi level [see Fig. 5]. For larger energies, in the right (K) valley of the dispersion relation [Fig. 3(a,c)] the number of modes carrying the current to the right is by 1 larger than the number of modes carrying the current to the left [Fig. 3(c)]. Hence, even for a strong but long-range perturbation the ribbon carries current at least in a single mode^{17,18} unless the tip raises the edge potential to the Fermi level – as it is still the case in Fig. 5(a,b) also beyond the single subbands transport conditions.

In Figure 8 we plotted the backscattering probabilities for the parameters of the tip of Fig. 5(a) (large and wide tip potential $V = 0.5$ eV, $d = 40$ nm) for the E_F range with three subbands or six wave vectors at the Fermi energy [Fig. 3(b-c)]. The intervalley scattering in the lowest subband (of probability $R_{1'1}$ corresponding to the change of the wave vector from k'_{1+} to k_{1-} – see Fig. 3(b,c)) occurs only for the tip near the edge of the ribbon [Fig. 8(a)], but when it does, it is nearly complete ($R_{1'1} \simeq 1$). The other intervalley scattering paths $R_{1'2}$ [Fig. 8(c)], $R_{2'2}$ [Fig. 8(e)], $R_{2'2'}$ [Fig. 8(f)] occur also for the tip near the edge but with smaller probabilities. The effective backscattering channels for the tip in the center of the ribbon are $R_{2'2'} = R_{22}$ [Fig. 8(d)] that appear within the same parabolic subbands [Fig. 3(b,c)]. The backscattering by the tip in the $k'_{2+} \rightarrow k'_{2-}$ channel governs the current and scattering density pattern that is displayed in Fig. 7(c-f). The oscillations at the left to the tip are due to the interference between $k_{2'_+}$ and $k_{2'_-}$ eigenstates and correspond to the period of $\frac{2\pi}{|k_{2'_+} - k_{2'_-}|}$, which is equal to 103\AA and 58\AA for $E_F = 0.3$ and 0.4 eV, respectively. The conductance of the ribbon raises from 1 to 3 for E_F above 0.2 eV [see the dashed lines in Fig. 5] with backscattering by the tip in the $2'_+ \rightarrow 2'_-$ channel

disappearing at higher Fermi energies, [cf. Fig. 5(e)].

B. Armchair ribbons

The armchair edges of the ribbons strongly mix the valleys and the zero point energy appears only for a single wave vector in the dispersion relation for metallic channels [Fig. 3(d)] or a single extremum per energy band is observed [Fig. 3(g)] for the semiconducting channel.

For the semiconducting armchair ribbon we find that the tip strictly blocks the current for any low E_F [region '1' in Fig. 9(b)] while the metallic ribbon ignores the presence of the tip in the single-subband transport conditions [region '1' in Fig. 9(a)]. In contrast to the case of the zigzag ribbon, the conductance is a smooth function of both E_F and the tip position. The low-energy results are given in Fig. 4 with $T = 1$ for the metallic ribbon for both $E_F = 0.07$ eV and $E_F = 0.13$ eV, irrelevant of the tip position. The metallic armchair ribbon possesses a perfectly conducting channel due to the pseudovalley symmetry⁴⁶, conserved at low energy, hence the absence of backscattering in the lowest subband transport. For the semiconducting armchair ribbon the tip blocks the current for any tip position above the ribbon [$E_F = 0.07$ eV in Fig. 4(a)] or reduces it strongly, particularly near the center of the ribbon [$E_F = 0.1$ eV in Fig. 4(b)]. In general, the most effective backscattering channel is the one within the same subband [$k_{2+} \rightarrow k_{2-}$, $k_{3+} \rightarrow k_{3-}$] and for the tip above the center of the ribbon.

At higher energies, for the semiconducting ribbon, only the backscattering within the same subband is non-negligible [Fig. 10(d-f)], including the non-zero channel in the lowest subband. For the metallic ribbon the backscattering within the lowest subband is absent due to the pseudovalley symmetry⁴⁶. Scattering in the same subband [Fig. 10(b-c)] is the strongest as in the semiconducting case and it is most effective for the tip above the center of the ribbon [Fig. 10(b-f)]. For the metallic ribbon a non-zero scattering between the subbands is also found [Fig. 10(a)] but only for the tip near the edges of the ribbons. In Fig. 4(c) we plotted a cross section of Fig. 5(c) and Fig. 9 for Fermi energies in multiple subband transport regime. For higher Fermi energies, the tip can no longer form the n-p junction at the edge, and the characteristic backscattering of the zigzag ribbon is not observed.

Summarizing, for higher Fermi energies the overall response of the ribbon conductance to the tip position is qualitatively similar for all ribbon types, i.e. it is smooth and maximal at the center of the ribbon. The $T(y_t)$ dependence can be approximately put in a $(y_t - D/2)^\alpha$ form with α that strongly varies with the energy for any type of the edge, D being the width of the ribbon. For higher Fermi energies the response of the ribbon to the tip scanning its surface is qualitatively independent of the type of the boundary, in spite of the fact that the current and density distributions are distinctly different [Fig. 4(f,i)].

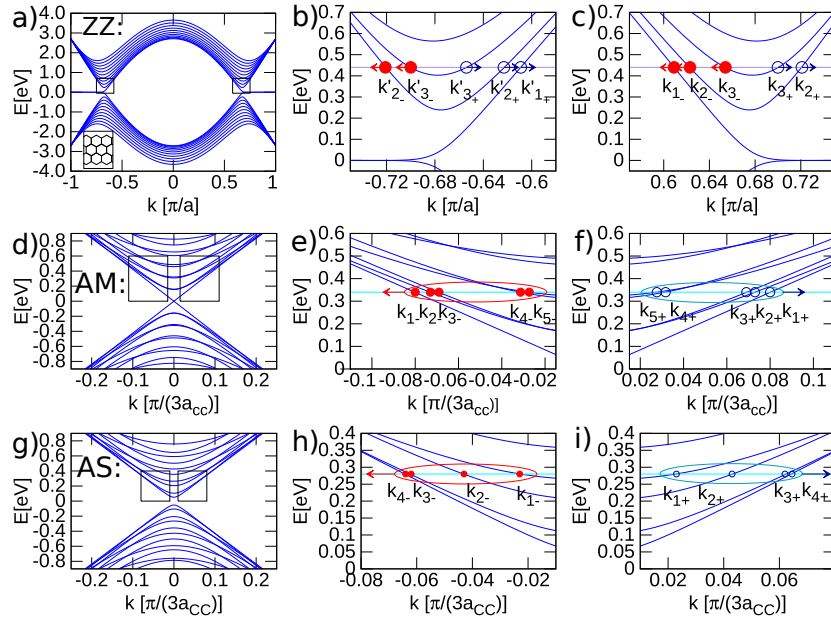


FIG. 3: (a) Dispersion relation for a zigzag nanoribbon 102 atoms wide. (b,c) Enlarged fragments marked by rectangles in (a). The arrows indicate the current direction. (d-f) same as (a-c) only for a metallic armchair ribbon with 92 atoms across the channel. (g-h) same as (a-c) only for a semiconducting armchair ribbon with 93 atoms across the channel. Arrows in (b,c,e,f,g,h) indicate the direction of the current flow. Here and in the other figures ZZ, AM, and AS stand for zigzag, armchair metallic and armchair semiconducting ribbons.

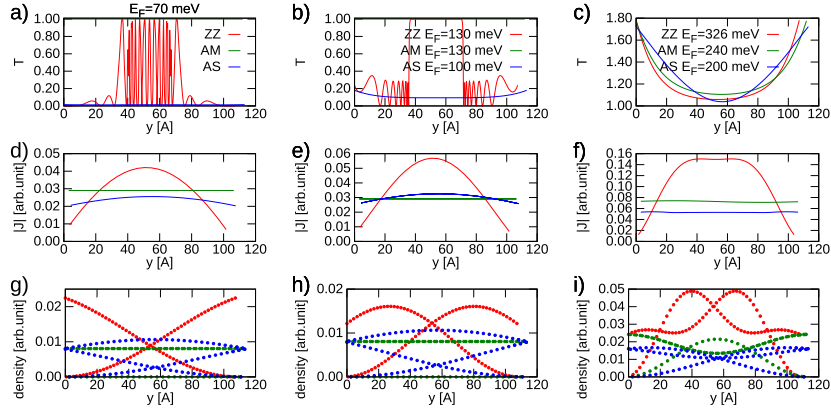


FIG. 4: (a-c) The transfer probability as a function of the tip position for $V_t = 0.2$ eV and $d = 40a$. (d-f) The density current averaged over neighbor cells. (g-i) The probability density for ribbons without the tip. In the left column (a,d,g) $E_F = 0.7$ eV and in the middle (b,e) $E_F = 0.13$ eV for zigzag and armchair metallic and (h) $E_F = 0.1$ eV for armchair semiconducting. Red lines correspond to a zigzag ribbon with 102 atoms across the channel, green (blue) to the metallic (semiconducting) armchair ribbons with 92 (93) atoms across the channel. In (c,f,i) results for higher energies are given. For the corresponding dispersion relation see Fig. 3(a-c) for the zigzag ribbon, and Fig. 3(d-f) for metallic and Fig. 3(g-i) for semiconducting nanoribbons.

IV. NARROWING OF THE RIBBON

As an intermediate step towards description of QPCs let us consider the channel of varied width that is depicted in the inset to Fig. 11. The channels at both sides of connection (A, B and E, F in Fig. 11) as well as the linking edges (C, D in Fig. 11) are assumed of the same type (zigzag or armchair). Short segments of varied type of the edge appear at the connections between the hor-

izontal and slanted ends of the ribbon (see the inset in Fig. 12(i)).

Figure 11 shows the conductance of the contact as a function of the Fermi energy for both zigzag and armchair edges. The conductance exhibits a very neat quantization as a function of the Fermi energy. A pronounced quantization of conductance⁴³ is generally difficult to obtain in graphene quantum point contacts (see Introduction). According to the results of Fig. 11 a channel contain-

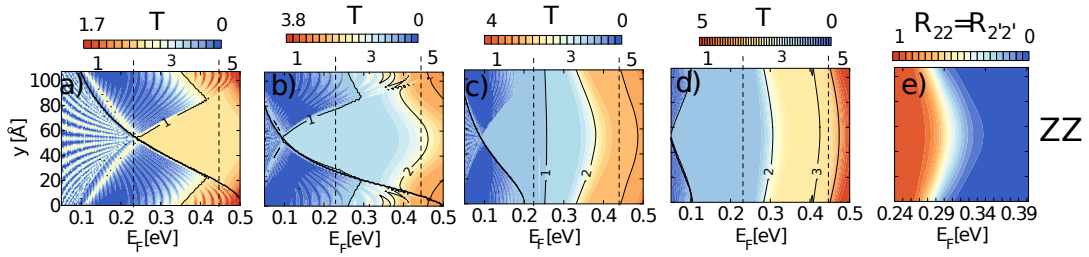


FIG. 5: Conductance of the zigzag ribbon with dispersion relation of Fig. 3 as a function of the position of the tip and the Fermi energy. Parameters of the tip $V_t = 0.5$ eV, $d = 40a$ (a), $V_t = 0.5$ eV, $d = 20a$ (b), $V_t = 0.2$ eV, $d = 40a$ (c), $V_t = 0.1$ eV, $d = 40a$ (d-f). The dashed lines separate regions of a varied number of subbands at the Fermi level – given above the upper axis. The thick black line in (a-d) corresponds to the tip positions for which the potential at the edge is raised to the Fermi energy.

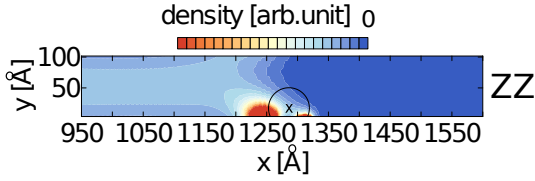


FIG. 6: Scattering probability density for $V_t = 0.2$ eV and $d = 40a$ at $E_F = 130$ meV and the tip near the lower edge of the ribbon (cross). The circle corresponds to potential introduced by the tip equal to E_F .

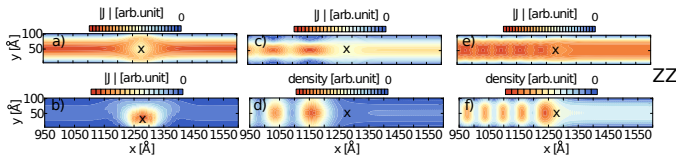


FIG. 7: (a,b) Amplitude of the current for the zigzag ribbon for $V_t = 0.2$ eV, $d = 40a$ for energy $E_F = 130$ meV in the lowest subband transport and the tip in the center of the ribbon (a) – for which $T = 1$ and near the lower edge (b) of the ribbon [$T = 0$]. (c-f) results for three subbands at the Fermi level for the amplitude of the current (c,e) and the scattering density (d,f) for $E_F = 0.3$ eV and $E_F = 0.4$ eV. The summed transfer probability is 1 at (c,d) and 3 at (e,f).

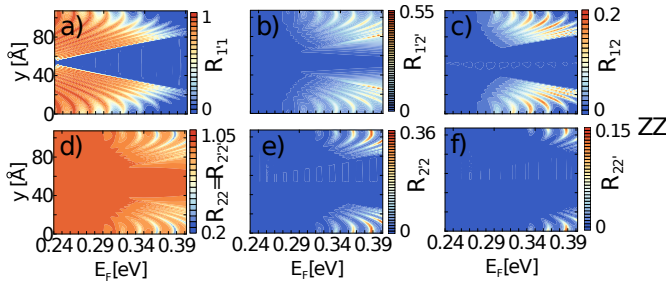


FIG. 8: Intersubband backscattering probabilities for parameters of Fig. 5(a) a) $R_{1'1}$, b) $R_{1'2'}$, c) $R_{1'2}$, d) R_{22} , e) $R_{2'2'}$, f) $R_{2'2}$ for $V_t = 0.5$ eV, $d = 40a$.

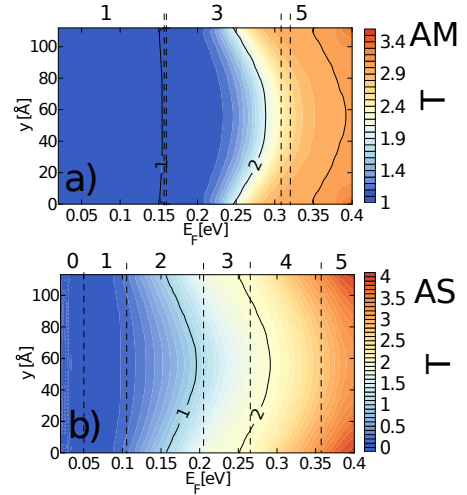


FIG. 9: Conductance versus the E_F and tip position for a metallic (a) and semiconducting (b) nanoribbons for $V_t = 0.2$ eV, and $d = 40a$. The dashed lines separate the regions with varied number of subbands at the Fermi level.

ing a narrowing is a good candidate for observation of conductance quantization in graphene systems.

A. Zigzag system

Let us consider the narrowing of the ribbon with zigzag edges. At low Fermi energy of 50 meV the connection of zigzag edges has a very low conductance of $T = 0.006$ [see the orange line in Fig. 11]. The ribbons at both sides of connection contain a perfectly conducting channel, but the inhomogeneity of the width leads to a very strong backscattering. At the connection of the zigzag edges a short sequence of an armchair form appears [see the arrow in Fig. 12(i)], which opens the intervalley backscattering channel. The tip potential above any of the two points closes the intervalley backscattering channel, allowing for the electron passage to the wider ribbon [Fig. 12(a,b,i,j)]. When the tip is close to the zigzag edges, it produces a

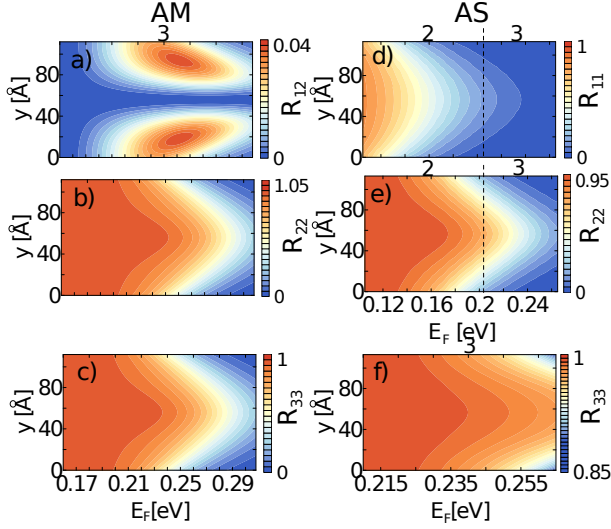


FIG. 10: Intersubband scattering probabilities for armchair metallic (a,b,c) and semiconducting (d,e,f) nanoribbons for $V_t = 0.2$ eV, $d = 40a$. The number of subbands at the Fermi level is given above the plots. For the metallic ribbon (a-c) R_{11} is zero.

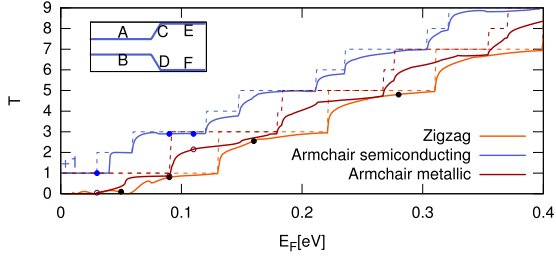


FIG. 11: Conductance at the contact between channels of varied widths (inset). The channels at the left (A,B) and right (E,F) hand side of connection and the edge at the variation of the width (C,D) are of the same type : zigzag or armchair. The lines show the conductance for zigzag, armchair metallic and semiconducting (offset by 1 in T) armchair edges of the channels. The number of atoms across the narrow (wide) channels is 188 (564) for the zigzag system, 161 (363) for metallic armchair channels and 163 (365) for semiconducting armchair edges. The dots on the lines indicate the points for which the SGM scans of Figs. 12 and 14 were calculated.

rapid variation of conductance which is related to formation of the n-p connection at the edge as discussed above. Note, that this applies not only for the narrower ribbon, but also at the widening and at the wider ribbon. Thus the probe resolves the zigzag edges in the entire system. The strong conductance response near the scattering centers localized at the edges are the counterparts of the conductance halos found in SGM mapping of graphene constrictions¹⁰. For the tip above the center of the narrower ribbon in Fig. 12(b) the potential at the edge stays below the Fermi level and the presence of the tip is not

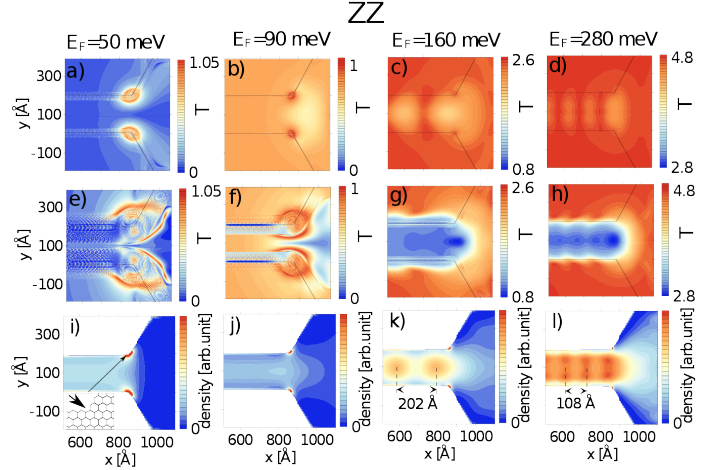


FIG. 12: Conductance maps for connection of zigzag channels of varied widths for $V_t = 0.1$ eV and $d = 20a$ (a-d) and $V_t = 0.2$ eV and $d = 40a$ (e-h). Panels (i-l) show the scattering probability density for the electron incident from the left in the absence of the tip. By arrows in (k,l) we indicated the period of the probability density oscillation which corresponds closely to the values expected for the backscattering within the last subband (see text). The inset to Fig. 12(i) shows the atomic structure of the turn of the edge with a short armchair segment that induces backscattering at low Fermi energy.

resolved in the map which is flat in the interior of the narrow ribbon [Fig. 12(c,f)]. The insensitiveness of conductance to the tip position in the center of the narrow channel and the rapid variation at the zigzag edge – are consistent with the properties of the zigzag ribbons for low Fermi energies discussed above.

For higher energies the effects of the edges are no longer present in the conductance maps [Fig. 12(c,d,g,h)]. Instead we observe – particularly for the lower potential at the tip [Fig. 12(c,d)] an appearance of a periodic oscillation of conductance. For instance the T maxima in the SGM maps are spaced by 202\AA for $E_F = 0.160$ eV and coincide with the minima of $R_{2'2'} = R_{22}$ backscattering. The T maxima are spaced by a characteristic wavelength for the intersubband scattering $\Delta x = \frac{2\pi}{|k_{2+} - k_{2-}|}$. The wave vectors are equal to $k_{2+} = 0.6825\frac{\pi}{a}$ and $k_{2-} = -0.6582\frac{\pi}{a}$ for $E_F = 0.160$ eV, producing spacing Δx equal to 202.3\AA , in a perfect agreement with the oscillation period found in the SGM map. For larger V_t and wider d a deviation from this perfect agreement is found due to variation in the wavelengths induced by the external potential of the tip and backscattering involving a larger number of subbands. In particular in Fig. 12(g) for $V_t = 0.2$ eV the transport is reduced to the lowest subband ($T = 1$) for the tip above the channel and the oscillations disappear in the SGM map which takes the form similar to the one found for lower Fermi energy – Fig. 12(a,b).

The oscillations of the scattering density observed above for the uniform ribbons [see Fig. 7] resulted from

the presence of the tip but were not resolved by the conductance mapping. For the non-uniform ribbons the oscillations appear in the scattering wave functions due to the inhomogeneity of the channels already in the absence of the probe [Fig. 12(k,l)] and according to the present results they can be resolved by the scanning gate microscopy.

The number of subbands that appear at the Fermi level increases with the energy and several backscattering channels appear. For $E_F = 280$ meV [Fig. 12(d)] the spacing between the extrema of T map are $\simeq 108\text{\AA}$. The backscattering probabilities are displayed in Fig. 13. The SGM map T for $E = 280$ meV inside the channel [see Fig. 12(d)] is very well correlated to spatial variation of backscattering $R_{3'3'} = R_{33}$. The oscillation period resulting from the difference of the wave vectors is 107.23\AA with a perfect agreement with the spacing of T extrema in the SGM map. The intervalley scattering [$R_{3'3}$ in Fig. 13(b)] – gives only an enhanced backscattering at the exit from the thinner channel with no pronounced oscillation within. We find as a general rule, that – at least for a moderate tip potential [$V_t = 0.1$ eV, $d = 20a$] – the oscillations of conductance are observed as a function of the tip position inside the zigzag thinner channel and have periodicity corresponding to the backscattering within the highest subband.

B. Armchair systems

Figure 14 displays the T maps for the armchair edges of the narrowing [see the inset to Fig. 11]. At low energy the conductance of both metallic and semiconducting ribbons is nearly zero [Fig. 11]. Figure 14(a,d) indicates that similarly as for the zigzag system at low energy [Fig. 12(a,b)] the conductance is raised when the tip is located at the turns of the edges: at connection of the slanted edge to the thinner (for the metallic ribbon Fig. 14(a)) or wider (for semiconducting ribbons Fig. 14(d)) armchair channel.

For $E_F = 90$ meV and the thin semiconducting ribbon we have already two subbands at the Fermi level [Fig. 11] and the T map contains a clear oscillation [Fig. 14(e)] of periodicity characteristic to the backscattering in the uppermost subband. For the metallic [Fig. 14(b)] ribbon at this energy the thinner ribbon is still in the single subband transport conditions, no oscillations occur – exactly as for the zigzag ribbon for low Fermi energy [see Fig. 12(a-b,e-f)]. For armchair systems at $E_F = 90$ meV no edge effects are observed and the backscattering occurs only for the tip near the exit from the thin channel. The oscillations for the metallic ribbon occur when the next subbands enter below the Fermi energy [Fig. 11] – see Fig. 14(c), with the periodicity characteristic generally to backscattering within the highest subband with the period of $\frac{2\pi}{|k_{l+} - k_{l-}|}$ for l being the index of the last subband. There are exceptions to this rule, in particular when the subband is very close to the Fermi energy the

backscattering of the subband can be nearly complete, then the one which is observed in the oscillation is not the highest but the next lower one.

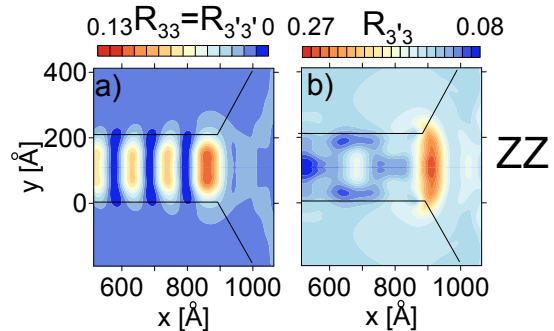


FIG. 13: Intraband (a) and intervalley (b) backscattering for the zigzag narrowing with the Fermi energy of 280 meV for $V_t = 0.1$ eV, $d = 20a$.

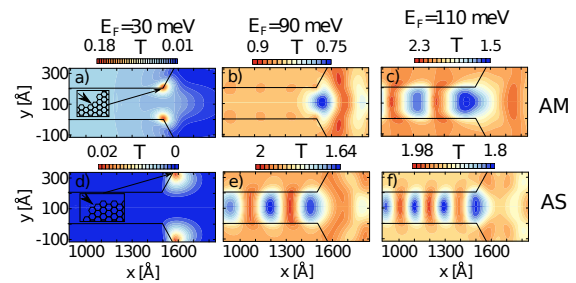


FIG. 14: T maps for a narrowing with armchair edges: metallic (a-c) and semiconducting (d-f) for $V_t = 0.1$ eV and $d = 20a$. The insets in a) and d) display the fragments of the edges near the exit from the narrower channel and the entrance to the wider channel, respectively where a short segment of zigzag edge appears, leading to the strong backscattering which is neutralized by the probe potential as in Fig. 12 above.

V. QUANTUM POINT CONTACTS

A. Long narrowing of QPC

We are now ready to proceed to description of SGM maps for quantum point contacts formed within the graphene ribbons. We first consider a system based on two narrowings of the channels as described above, in the form given in the inset to Fig. 15 with a finite length L of the narrower ribbon. We assume that the narrower ribbon has a width $d_n \simeq 20$ nm and consider L between 32 nm and 58 nm, for the transverse size of the wider ribbon between 44 nm and 60 nm. The conductance of all the considered ribbons – zigzag and armchair – both semiconducting and metallic – drops to zero for low E_F .

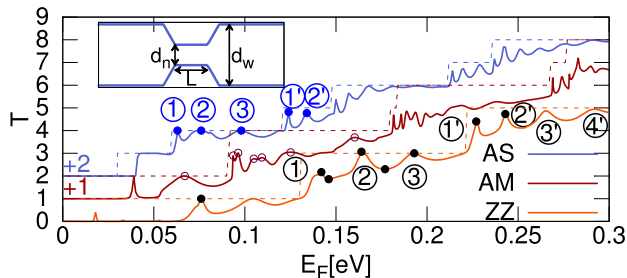


FIG. 15: Transfer probability as a function of Fermi energy for QPC with long constriction (inset). The dashed lines represent the transfer probability in graphene ribbon of the same width as the constriction. The conductance for armchair ribbons is shifted by 1 for the metallic system and 2 for semiconducting system. The lengths indicated in the inset are $L = 577$ Å, $d_n = 199.26$ Å and $d_w = 447.72$ Å for the armchair semiconducting ribbon, $L = 551$ Å, $d_n = 196.8$ Å and $d_w = 445.26$ Å for the armchair metallic ribbon and $L = 320$ Å, $d_n = 198.8$ Å and $d_w = 599.24$ Å for the zigzag ribbon.

The inhomogeneity of the ribbon leads in this way to appearance of the transport gap⁴⁰ for any type of the edge of the wider ribbon.

The conductance of the QPC with zigzag edges is displayed in Fig. 15 with the solid orange line, while the dashed orange line indicates the conductance of the narrow part of the system (the number of subbands carrying the current to the right at the Fermi level). The conductance of the narrower QPC is generally lower than the conductance of the narrower part with exceptions of a series of conductance peaks. In Fig. 16 we plotted the scattering probability density [Fig. 16(ai-ap)] and the SGM maps [Fig. 16(aa-ah)] for the zigzag QPC and a number of chosen Fermi energies marked in Fig. 15 with points. In the T maps we find a pronounced variation of conductance maps within the narrower part of the ribbon. Outside the constriction the conductance maps are almost flat. No conductance variation of visible in the scale of the variations within the narrower channel. For the low-energy peak $E_F = 76$ meV – within a single subband of the narrow channel – the conductance map of the system drops when the probe is located within the constriction [Fig. 16(aa)]. In the scattering densities and conductance maps we find signatures of backscattering at the turns of the edges as discussed above for the asymmetric narrowing of the channel [Fig. 16(aa)]. For higher energies [Fig. 16(ab-ah)] the corners correspond to high values of the probability densities but with no counterparts in the SGM map – again as in the asymmetric narrowing of Fig. 12.

For higher Fermi energies, within each segment of E_F corresponding to a fixed number of subbands of the narrow channel (dashed orange line in Fig. 15 we observe that 1) at the first maximum of $T(E_F)$ at the low energy side the conductance map contains a single mini-

mum along the channel, 2) each subsequent T peak that is higher at the E_F scale corresponds to conductance map with a number of minima increased by 1. A representative example is given in Fig. 16(ab-ad) for the T maps for the first, second and the third T maxima of conductance [see the numbers near the orange line in Fig. 15]. The conductance resonances correspond to an integer number of the scattering wavelengths for the highest subband within the constriction with maxima observed in the scattering probability density [cf. Fig. 16(aj-al)]. Once another subband falls below the Fermi energy (for instance above $E_F = 0.2$ eV) another sequence of conductance peaks is formed with the number of maxima within the constriction starting from 1 again (see the peaks labeled by primed numbers and maps of Fig. 16(ae,af)). Beyond the resonances this regular correspondence between the scattering density and the conductance map is lost [cf. Fig. 16(ag,ah) for energies $E_F = 146$ meV and $E_F = 177$ meV].

The properties of the QPCs with armchair edges and the width corresponding to a semiconducting dispersion relation turn out to be similar to those of the zigzag system, with pronounced $T(E_F)$ peaks [cf. blue solid line in Fig. 15] corresponding to a determined number of maxima of the probability density correlated with the conductance maps. For the metallic armchair system $T(E_F)$ dependence is more complex [red line in 15]. In particular we find that the peaks corresponding to a fixed number of extrema of the probability density and SGM maps appear in pairs [cf. Fig. 16(l,m) for $E_F = 93.5$ meV and $E_F = 96.3$ meV for a single extremum, and Fig. 16(n,o) for $E_F = 104.9$ meV and $E_F = 109.3$ meV for the double extremum, etc.].

The difference in the properties of semiconducting and metallic armchair systems has its source in the details of the dispersion relation. When a subsequent subband for the electron transport is opened within the narrow channel, the subbands of the metallic ribbon are nearly degenerate [see Fig. 3(d) for low k] while for the armchair ribbon the subbands are split near zero wave vector [see Fig. 3(g)]. Thus, for the metallic ribbon we have two close highest subbands of similar Fermi wavelengths, inducing formation of separate but close resonances for both. The neighborhood of the wavelengths enhances the intersubband scattering leading to a complex form of $T(E_F)$ at higher energies.

Concluding, for QPCs with a long constriction the conductance peaks of $T(E_F)$ dependence are related to resonances of the highest subband, and the resonant density within the constriction is resolved by the SGM conductance maps. The tip potential enhances the backscattering within the highest – nearly parabolic – subband. The tip-induced backscattering is most effective in the region where the scattering probability density is maximal. The zigzag and semiconducting narrowing display a distinct regularity in the subsequent number of peaks and the form of the SGM map. For the metallic armchair ribbon the $T(E_F)$ dependence is more complex due to the near

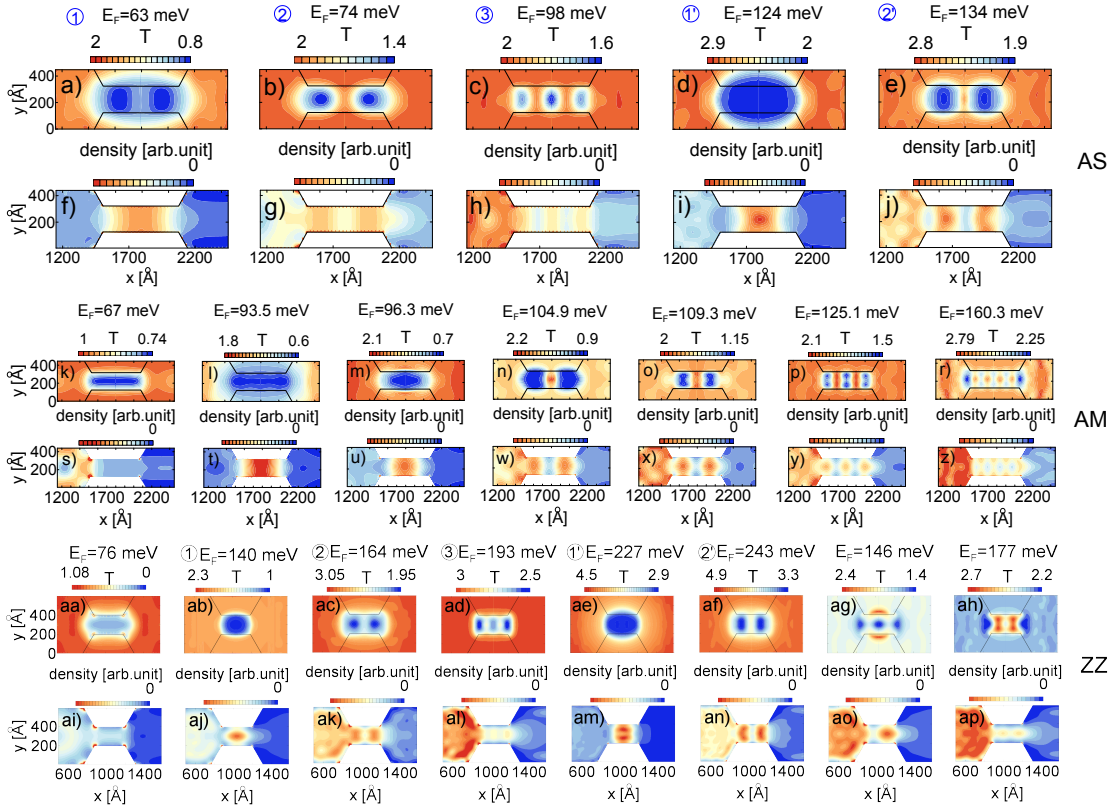


FIG. 16: T maps for a long QPC with zigzag edges (a-d) and scattering densities (e-h) at the Fermi energies corresponding to the maxima of transmission probability. Parameters of the tip: $V_t = 0.1$ eV, $d = 20a$.

degeneracy of the highest subbands near their bottom and pairs of resonances with similar conductance maps are found. For each system, outside the constriction the conductance map is almost flat.

B. Short constriction

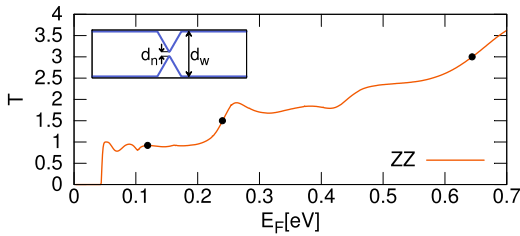


FIG. 17: Transfer probability as a function of Fermi energy for wedge-shaped QPC (inset). The widths indicated in the inset are $d_n = 58$ Å, $d_w = 598.8$ Å.

Let us consider the QPC with a short constriction. We studied first a wedge shaped constriction of a zigzag ribbon depicted in the inset to Fig. 17, with the ribbon narrowing from about 60 nm to about 6 nm. The con-

ductance of the QPC is displayed in the main panel of Fig. 17. The short constriction cannot support any localized resonances in the form discussed above, and the corresponding series of $T(E_F)$ peaks are not observed. For any Fermi energy a minimum is found in the SGM map within the constriction and only a low variation of conductance outside the constriction is found – see the maps displayed in Fig. 18. Some variation outside the constriction is only observed for low E_F [Fig. 18(a)] and it disappears at higher energies in the scale of the variation in the narrow part. [Fig. 18(b,c)].

The results found for this short, narrow and abrupt QPC are reproduced also for a large smooth at the atomic scale constriction of a cosine profile²². The system exhibits²² a detectable smooth steps of conductance²¹ also when the constriction remains quite wide. The $T(E_F)$ result is presented in Fig. 19, where we considered wide ($d_w = 100$ nm to 150 nm) zigzag and semiconducting armchair edges that at the narrowest part have width of $d_n = 33$ nm to 50 nm.

The conductance maps for the zigzag ribbon are displayed in Fig. 20. In the scattering probability density maps we find maxima along the constriction [Fig. 20(e-h)]. The atomic steps forming constrictions contain multiple of zigzag-armchair short segments of the edges [Fig. 20(i)] – which as discussed above – lead to an effective backscattering. At low energy [$E_F = 25$ meV in Fig.

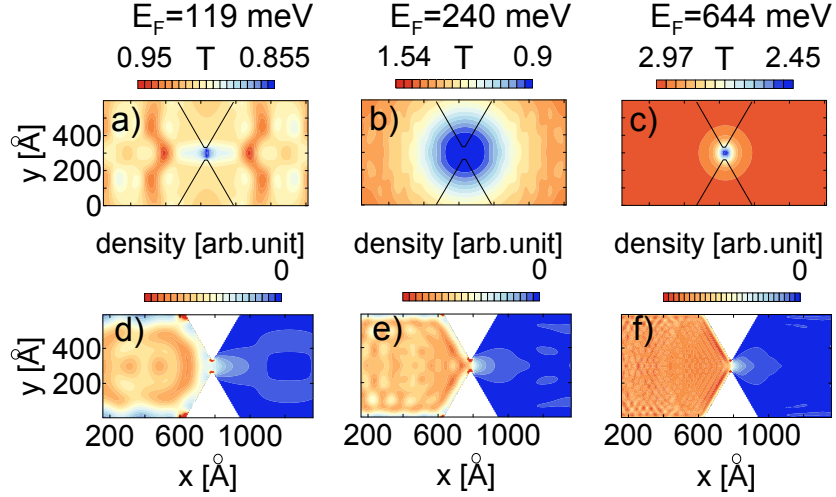


FIG. 18: T maps for a wedge-shaped QPC with zigzag edges (a-c) and scattering densities (d-f). Parameters of the tip: $V_t = 0.1$ eV, $d = 20a$.

20(a)] the tip neutralizes the backscattering when located above these parts of the edges – in consistence with the results for asymmetric narrowing [cf. Fig. 12(a,b)]. At higher energies [cf. Fig. 20(b-d)] we are left with a minimum of conductance at the center of the constriction and a low variation of conductance in the outside.

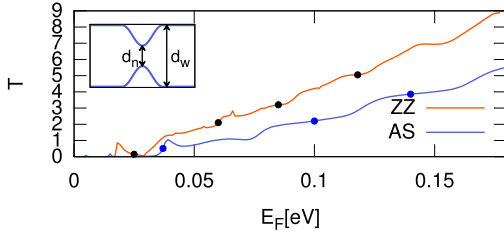


FIG. 19: Transfer probability as a function of Fermi energy for large QPC (inset). The widths indicated in the inset are $d_n = 497$ Å, $d_w = 1498.1$ Å for zigzag ribbons and $d_n = 332.1$ Å, $d_w = 998.76$ Å for armchair ribbons.

VI. SUMMARY AND CONCLUSIONS

We have performed an analysis of the conductance response of graphene nanoribbons and their narrowing to a perturbation introduced by potential of a scanning probe. The study was based on the tight binding implementation of the quantum transmitting boundary method.

We find that at low Fermi energies the response of the zigzag ribbons to the scanning probe occurs only for the tip above the edges of the channels due to formation of the local n-p junctions allowing for a very effective intervalley backscattering and producing rapidly varying con-

ductance maps. For the probe above the interior of the zigzag ribbon the conductance does not react to the perturbation. The finding is due to existence of the perfectly conducting channel and is also observed for metallic armchair ribbon irrespective of the position of the probe. For higher Fermi energies the response of the zigzag and armchair nanoribbons is similar producing smooth conductance maps as functions of the tip position with the strongest response in the center of the ribbon.

For the asymmetric narrowing of the ribbon – which exhibits a very distinct conductance quantization – the conductance maps at low energy resolve the zigzag edges and scattering centers near the zigzag-armchair segments which necessarily appear in atomic steps that form the narrowing. For higher Fermi energy an oscillation of the scattering probability density is observed, which in general corresponds to backscattering within the highest subband of the narrower channel. According to the present results the oscillation can be resolved in the maps of conductance response to the probe.

For quantum point contacts similar oscillations of conductance maps are observed for longer constrictions that are connected with resonant peaks of $T(E_F)$ dependence. Formation of conductance peaks have a regular reentrant character in the energy with subsequent subbands appearing at the Fermi level. The peaks correspond to scattering probability density and conductance map with a determined number of extrema along the constriction. Shorter constrictions that do not support the resonances within the narrowing produce a smooth $T(E_F)$ dependence with SGM maps producing a minima of conductance within the constrictions. For the asymmetric narrowing – at the wider part of the ribbon and for QPC outside the constriction no conductance response of the system is observed in the response maps.

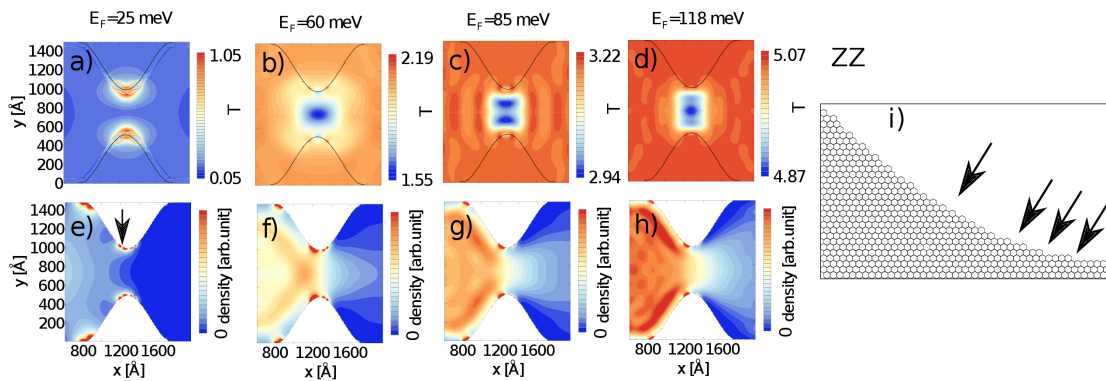


FIG. 20: T maps (a-d) for a large QPC with mesoscopically smooth edges within a zigzag nanoribbon and the corresponding scattering densities (e-h) in the absence of the probe. Parameters of the tip potential: $V_t = 0.1$ eV, $d = 20a$. (i) - enlarged fragment of the narrowing indicating armchair segments within the zigzag edge that are mainly responsible for the scattering at low Fermi energy and that are neutralized by the tip potential [see (a)].

- ¹ H. Sellier, B. Hackens, M.G. Pala, F. Martins, S. Baltazar, X. Wallart, L. Desplanque, V. Bayot, and S. Huant, *Sem. Sci. Tech.* **26**, 064008 (2011); D.K. Ferry, A.M. Burke, R. Akis, R. Brunner, T.E. Day, R. Meisels, F. Kuchar, J.P. Bird, and B.R. Bennett, *Sem. Sci. Tech.* **26**, 043001 (2011).
- ² K. E. Aidala, R. E. Parrott, T. Kramer, E. J. Heller, R. M. Westervelt, M. P. Hanson, and A. C. Gossard, *Nat. Phys.* **3**, 464 (2007).
- ³ B. J. LeRoy, A. C. Bleszynski, K. E. Aidala, R. M. Westervelt, A. Kalben, E. J. Heller, S. E. J. Shaw, K. D. Maranowski, and A. C. Gossard, *Phys. Rev. Lett.* **94**, 126801 (2005); M. P. Jura, M. A. Topinka, M. Grobis, L. N. Pfeiffer, K. W. West, and D. Goldhaber-Gordon, *Phys. Rev. B* **80**, 041303(R) (2009); M. P. Jura, M. Grobis, M. A. Topinka, L. N. Pfeiffer, K. W. West, and D. Goldhaber-Gordon, *Phys. Rev. B* **82**, 155328 (2010). N. Paradiso, S. Heun, S. Roddaro, L.N. Pfeiffer, K.W. West, L. Sorba, G. Biasiol, F. Beltram, *Physica E* **42**, 1038 (2010).
- ⁴ B. Brun, F. Martins, S. Faniel, B. Hackens, G. Bachelier, A. Cavanna, C. Ulysse, A. Ouerghi, U. Gennser, D. Mailly, S. Huant, V. Bayot, M. Sanquer, and H. Sellier, *Nature Communications* **5**, 4290 (2014).
- ⁵ F. Martins, B. Hackens, M. G. Pala, T. Ouisse, H. Sellier, X. Wallart, S. Bollaert, A. Cappy, J. Chevrier, V. Bayot, and S. Huant, *Phys. Rev. Lett.* **99**, 136807 (2007); M. G. Pala, B. Hackens, F. Martins, H. Sellier, V. Bayot, S. Huant, and T. Ouisse, *Phys. Rev. B* **77**, 125310 (2008).
- ⁶ R. Crook, C. G. Smith, A. C. Graham, I. Farrer, H. E. Beere, and D. A. Ritchie, *Phys. Rev. Lett.* **91**, 246803 (2003); A. M. Burke, R. Akis, T. E. Day, G. Speyer, D. K. Ferry, and B. R. Bennett, *Phys. Rev. Lett.* **104**, 176801 (2010).
- ⁷ R. Jalilian, L. A. Jauregui, G. Lopez, J. Tian, C. Roecker, M.M. Yazdanpanah, R.W. Cohn, I. Jovanovic, and Y.P. Chen, *Nanotechnology* **22**, 295705 (2011).
- ⁸ A.G.F. Garcia, M. König, D. Goldhaber-Gordon, K. Todd, *Phys. Rev. B* **87**, 085446 (2013).
- ⁹ S. Schnez, J. Güttinger, M. Huefner, C. Stamper, K. Ensslin, and T. Ihn, *Phys. Rev. B* **82**, 165445 (2010).
- ¹⁰ M.R. Connolly, K.L. Chiu, A. Lombardo, A. Fasoli, A.C. Ferrari, D. Anderson, G.A.C. Jones, and C.G. Smith, *Phys. Rev. B* **83**, 115441 (2011).
- ¹¹ J. Berezovsky, M.F. Borunda, E.J. Heller, and R.M. Westervelt, *Nanotechnology* **21**, 274013 (2010).
- ¹² J. Berezovsky and R.M. Westervelt, *Nanotechnology* **21**, 274014 (2010).
- ¹³ D. Cabosart, S. Faniel, F. Martins, B. Brun, A. Felten, V. Bayot, and B. Hackens, *Phys. Rev. B* **90**, 205433 (2014).
- ¹⁴ B.J. van Wees, H. van Houten, C.W.J. Beenakker, J.G. Williamson, L.P. Kouwenhoven, D. van der Marel, C.T. Foxton, *Phys. Rev. Lett.* **60**, 848 (1988).
- ¹⁵ T. Anto, T. Nakanishi, and R.Saito, *J. Phys. Soc. Jpn.* **67**, 2857 (1998); V.V. Cheianov and V.I. Fal'ko, *Phys. Rev. B* **74**, 041403(R) (2006);
- ¹⁶ M.I. Katsnelson, K.S. Novoselov, and A.K. Geim, *Nature Phys.* **2**, 620 (2006). C.W.J. Beenakker, *Rev. Mod. Phys.* **80**, 1337 (2008).
- ¹⁷ K. Wakabayashi, Y. Takane, and M. Sigrist, *Phys. Rev. Lett.* **99**, 036601 (2007).
- ¹⁸ K. Wakabayashi, Y. Takane, M. Yamamoto, and M. Sigrist, *Carbon* **47**, 124 (2009).
- ¹⁹ R. Yang, L. Huang, Y.-C. Lai, and C. Grebogi, *Phys. Rev. B* **84**, 035426 (2011).
- ²⁰ Y.M. Lin, V. Perebeinos, Z.H. Chen, and P. Avouris, *Phys. Rev. B* **78**, 161409(R) (2008).
- ²¹ N. Tombros, A. Veligura, J. Junesch, M.H.D. Guimarães, I.J. Vera-Marun, H.T. Jonkman, and B.J. van Wees, *Nat. Phys.* **7**, 697 (2011).
- ²² S. Ihnatsenka and G. Kirczenow, *Phys. Rev. B* **85**, 121407(R) (2012).
- ²³ M.Y. Han, B. Özyilmaz, Y. Zhang, P. Kim, *Phys. Rev. Lett.* **98**, 206805 (2007).
- ²⁴ Z.H. Chen, Y.M. Lin, M.J. Rooks, P. Avouris, *Physica E* **40**, 228 (2007).
- ²⁵ F. Molitor, A. Jacobsen, C. Stampfer, J. Güttinger, T. Ihn, K. Ensslin, *Phys. Rev. B* **79** 075426 (2009).
- ²⁶ L. Brey, and H.A. Fertig, *Phys. Rev. B* **73**, 235411 (2006).
- ²⁷ D.A. Areshkin, D. Gunlycke, and C.T. White, *Nano Lett.* **7**, 204 (2007).
- ²⁸ K. Wakabayashi, Y. Takane, M. Yamamoto, and M. Sigrist,

- New J. Phys **11**, 095016 (2009).
- ²⁹ Y.W.Son, M.L. Cohen. and S.G. Louie, Phys. Rev. Lett. **97**, 216803 (2006).
- ³⁰ K. Nakada, M. Fujita, G. Dresselhaus, and M. S. Dresselhaus, Phys. Rev. B **54**, 17954 (1996).
- ³¹ M.D. Petrovic and F.M. Peeters, Phys. Rev. B **91**, 035444 (2015).
- ³² S. Neubeck, L.A. Ponomarenko, A.S. Mayorov, S.V. Morozov, R. Yang, and K.S. Novoselov, Physica E **44**, 1002 (2012).
- ³³ N. Pascher, D. Bischoff, T. Ihn, and K. Ensslin, Appl. Phys. Lett. **101**, 063101 (2012).
- ³⁴ J. Wurm, M. Wimmer, I. Adagidelli, K. Richter, and H.U. Baranger, New J. Phys. **11**, 095022 (2009).
- ³⁵ X. Jua, M. Hofmann, V. Meunier, B.G. Sumpter, J. Campos-Delgado, J. M. Romo-Herrera, H. Son, Y.-P. Hsieh, A. Reina, J. Kong, M. Terrones, M.S. Dresselhaus, Science **323**, 1701 (2009).
- ³⁶ A.R. Akhmerov, and C.W.J. Beenakker, Phys. Rev. B **77**, 085423 (2008).
- ³⁷ C.S. Lent and D.J. Kirkner, J. Appl. Phys. **67**, 6353 (1990).
- ³⁸ M. Wimmer and K. Richter, J. Comput. Phys. **228**, 8548 (2009).
- ³⁹ F. Muñoz-Rojas, D. Jacob, J. Fernández-Rossier, and J. J. Palacios, Phys. Rev. B **74**, 195417 (2006).
- ⁴⁰ M. Evaldsson, I. V. Zozoulenko, Hengyi Xu, and T. Heinzl, Phys. Rev. B **78**, 161407(R) (2008).
- ⁴¹ K. Kolasinski and B. Szafran, Phys. Rev. B **89**, 165306 (2014).
- ⁴² J. Tworzydło, B. Trauzettel, M. Titov, A. Rycerz, and C. W. J. Beenakker, Phys. Rev. Lett. **96**, 246802 (2006); A. Rycerz, J. Tworzydło, and C.W.J. Beenakker, Nature Physics **3**, 172-175 (2007).
- ⁴³ N.M.R. Peres, A.H. Castro Neto and F. Guinea, Phys. Rev. B **73**, 195411 (2006).
- ⁴⁴ K. Wakabayashi, Phys. Rev. B **64**, 125428 (2001).
- ⁴⁵ K. Kolasinski and B. Szafran, Phys. Rev. B **88**, 165306 (2013).
- ⁴⁶ J. Wurm, M. Wimmer, and K. Richter, Phys. Rev. B **85**, 245418 (2012).
- ⁴⁷ M. Zwierzycki, P. A. Khomyakov, A. A. Starikov, K. Xia, M. Talanana, P. X. Xu, V. M. Karpan, I. Marushchenko, I. Turek, G. E. W. Bauer, G. Brocks, and P. J. Kelly, Phys. Status Solidi B **245**, 623 (2008).

VII. APPENDIX

A. Channel eigenstates

The procedure for determining the dispersion relation and the Hamiltonian eigenstates for the nanoribbon channels is described here. For an infinite, uniform lead the tight-binding Hamiltonian can be put in a matrix⁴⁷

$$\mathbf{H} = \begin{pmatrix} \ddots & \dots & 0 & 0 & & \\ \vdots & \mathbf{H}_{u-1} & \mathbf{B}_{u-1}^\dagger & 0 & 0 & \\ 0 & \mathbf{B}_{u-1} & \mathbf{H}_u & \mathbf{B}_u^\dagger & 0 & \\ 0 & 0 & \mathbf{B}_u & \mathbf{H}_{u+1} & \vdots & \\ & 0 & 0 & \dots & \ddots & \end{pmatrix}, \quad (9)$$

where matrix \mathbf{H}_u concerns a single elementary cell u [see Fig. 2] and \mathbf{B}_u describes the connection between cells u and $u+1$. The \mathbf{H}_u and \mathbf{B}_u matrices have dimensions $n \times n$ where n is number of atomic orbitals within a single elementary cell. For ideally periodic nanoribbons forming the channels the matrices \mathbf{H}_u , \mathbf{B}_u are the same for all elementary cells, and we skip the u index in the following. The Hamiltonian eigenfunction inside the channel can be written in a form divided on separate cells

$$\boldsymbol{\psi} = \begin{pmatrix} \vdots \\ \psi_{u-1} \\ \psi_u \\ \psi_{u+1} \\ \vdots \end{pmatrix}, \quad (10)$$

where ψ_u is a vector of size n . The wavefunction satisfies,

$$-\mathbf{B}\psi_{u-1} + (\mathbf{E}\mathbf{I} - \mathbf{H})\psi_u + \mathbf{B}^\dagger\psi_{u+1} = 0. \quad (11)$$

Based on the Bloch form of the wave function [Eq. 2] we make the following substitution:

$$\psi_{u-1} = \chi, \quad \psi_u = \lambda\chi, \quad \psi_{u+1} = \lambda^2\chi,$$

for which

$$-\mathbf{B}\chi + \lambda(\mathbf{E}\mathbf{I} - \mathbf{H})\chi + \lambda^2\mathbf{B}^\dagger\chi = 0. \quad (12)$$

With

$$\eta = \lambda\chi$$

the eigenproblem can be put in form

$$\left[\begin{pmatrix} 0 & \mathbf{I} \\ -\mathbf{B} & \mathbf{E}\mathbf{I} - \mathbf{H} \end{pmatrix} - \lambda \begin{pmatrix} \mathbf{I} & 0 \\ 0 & \mathbf{B}^\dagger \end{pmatrix} \right] \begin{bmatrix} \chi \\ \eta \end{bmatrix} = 0. \quad (13)$$

The generalized ($2n \times 2n$) eigenproblem has $2n$ solutions: n left-going and n right-going modes – propagating or decaying.⁴⁷ For evanescent modes it is straightforward to identify right and left going modes. For right-going evanescent modes the eigenvalue satisfies $|\lambda_{+,n}| < 1$ and for left-going evanescent modes $|\lambda_{-,n}| > 1$. The propagating modes – for the Bloch waves of Eq. (2) have the form $\lambda_{\pm,n} = \exp(ik\Delta x)$, with a real k , hence $|\lambda_{\pm,n}| = 1$. For a given E we look for the values of $|\lambda| = 1$ and determine the corresponding wave vectors and the periodic functions χ . Finally, we evaluate the current flux (7) and determine the direction of propagation – the current flux is positive (negative) for right (left) going modes.

B. Determination of the scattering amplitudes

The scattering amplitudes of Eq. (4) and Eq. (5) are determined in the following manner. We evaluate the coefficients d_{in}^l multiplying (4) by a complex conjugate of $\chi^{k'}$:

$$\langle \chi^{k'} | \psi_0 \rangle = \sum_l (c_{in}^l \langle \chi^{k'} | \chi^{k'_+} \rangle + d_{in}^l \langle \chi^{k'} | \chi^{k'_-} \rangle). \quad (14)$$

Here we denote the inner product in discrete form $\langle A|B\rangle = \sum_j A_j^* B_j$. Defining vector \mathbf{A} with $\mathbf{A}_{l'} = \langle \chi^{k_{-}^{l'}} | \psi_0 \rangle$ and matrices $\mathbf{B}_{l',l} = \langle \chi^{k_{-}^{l'}} | \chi^{k_{+}^{l}} \rangle$, $\mathbf{S}_{l',l} = \langle \chi^{k_{-}^{l'}} | \chi^{k_{-}^{l}} \rangle$ Eq. (14) can be written in a matrix form

$$\mathbf{A} = \mathbf{B}\mathbf{c}_{in} + \mathbf{S}\mathbf{d}_{in}, \quad (15)$$

which implies

$$\begin{aligned} \mathbf{d}_{in}^l &= \sum_{l'} (\mathbf{S}^{-1})_{l,l'} \mathbf{A}_{l'} - \sum_{l',j} (\mathbf{S}^{-1})_{l,j} \mathbf{B}_{j,l'} \mathbf{c}_{in}^{l'} \\ \mathbf{d}_{in}^{l'} &= \sum_{l'} (\mathbf{S}^{-1})_{l,l'} \langle \chi^{k_{-}^{l'}} | \psi_0 \rangle - \mathbf{c}_{in2}^{l'}. \end{aligned} \quad (16)$$

$$\begin{aligned} \frac{1}{\Delta x} (\psi_{0,v} - \psi_{-1,v}) &= \sum_l (c_{in}^l \chi_v^{k_{+}^l} \frac{1}{\Delta x} (1 - e^{-ik_{+}^l \Delta x}) + d_{in}^l \chi_v^{k_{-}^l} \frac{1}{\Delta x} (1 - e^{-ik_{-}^l \Delta x})) = \\ &= \sum_l (c_{in}^l \chi_v^{k_{+}^l} \frac{1}{\Delta x} \Delta_{k_{+}^l} + d_{in}^l \chi_v^{k_{-}^l} \frac{1}{\Delta x} \Delta_{k_{-}^l}). \end{aligned}$$

Using (16) we transform this equation to obtain $\psi_{-1,v}$:

$$\psi_{-1,v} = \psi_{0,v} - \sum_l \left(\mathbf{c}_{in}^l \chi_v^{k_{+}^l} \Delta_{k_{+}^l} - \mathbf{c}_{in2}^{l'} \chi_v^{k_{-}^l} \Delta_{k_{-}^l} + \sum_{l'} (\mathbf{S}^{-1})_{l,l'} \langle \chi^{k_{-}^{l'}} | \psi_0 \rangle \chi_v^{k_{-}^l} \Delta_{k_{-}^l} \right) \quad (17)$$

Similarly, for the other end of the computational box we multiply equation (5) by the complex conjugate of $(\chi^{k_{+}^{l'}} e^{ik_{+}^{l'} N \Delta x})$:

$$\langle \chi^{k_{+}^{l'}} e^{ik_{+}^{l'} N \Delta x} | \psi_N \rangle = \sum_l \langle \chi^{k_{+}^{l'}} | \chi^{k_{+}^l} \rangle e^{i(k_{+}^l - k_{+}^{l'}) N \Delta x} \mathbf{c}_{out}^l = \sum_l \mathbf{S}'_{l',l} \mathbf{c}_{out}^l, \quad (18)$$

hence

$$\mathbf{c}_{out}^l = \sum_{l'} (\mathbf{S}'^{-1})_{l,l'} \langle \chi^{k_{+}^{l'}} e^{ik_{+}^{l'} N \Delta x} | \psi_N \rangle \quad (19)$$

The derivative at the end of the computational box is

$$\frac{1}{\Delta x} (\psi_{N+1,v} - \psi_{N,v}) = \sum_l c_{out}^l \chi_v^{k_{+}^l} e^{ik_{+}^l N \Delta x} \frac{1}{\Delta x} (e^{i(k_{+}^l) \Delta x} - 1) \quad (20)$$

Then, using (19) we obtain:

$$\psi_{N+1,v} = \psi_{N,v} + \sum_{l,l'} (\mathbf{S}'^{-1})_{l,l'} \langle \chi^{k_{+}^{l'}} e^{ik_{+}^{l'} N \Delta x} | \psi_N \rangle \chi_v^{k_{+}^l} e^{ik_{+}^l N \Delta x} (e^{i(k_{+}^l) \Delta x} - 1) \quad (21)$$

The boundary conditions given by (17) and (21) are used as expressions for the wave functions outside of the computational box in the Schrödinger equation $H\psi = E\psi$. Having calculated the wavefunction ψ , we can calculate the coefficients d_{in}^l from (16) and c_{out}^l from (19). The results are next used for evaluation of the scattering probabilities and conductance in the Landauer approach.
